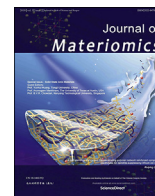


Contents lists available at [ScienceDirect](https://www.sciencedirect.com)

Journal of Materiomics

journal homepage: www.journals.elsevier.com/journal-of-materiomics/

Scalable microfabrication of three-dimensional porous interconnected graphene scaffolds with carbon spheres for high-performance all carbon-based micro-supercapacitors

Yiming Chen^a, Minghao Guo^a, Liang He^{a,b,*}, Wei Yang^a, Lin Xu^a, Jiashen Meng^a, Xiaocong Tian^{a,c}, Xinyu Ma^a, Qiang Yu^a, Kaichun Yang^d, Xufeng Hong^a, Liqiang Mai^{a,**}

^a State Key Laboratory of Advanced Technology for Materials Synthesis and Processing, International School of Materials Science and Engineering, Wuhan University of Technology, Wuhan, 430070, China

^b Department of Materials Science and NanoEngineering, Rice University, Houston, TX, 77005, United States

^c Faculty of Materials Science & Chemistry, China University of Geosciences, Wuhan, 430074, China

^d Department of Civil Engineering, Rice University, Houston, TX, 77005, United States

ARTICLE INFO

Article history:

Received 30 September 2018

Received in revised form

19 November 2018

Accepted 21 November 2018

Available online 11 December 2018

Keywords:

Three-dimensional

Injecting

Freeze-drying

Mass loading

Supercapacitor

ABSTRACT

As one of the most important micro energy storage devices (MESDs), graphene-based micro-supercapacitors (G-MSCs) possess the advantages of excellent flexibility, long cycle life, affordability and high reliability. In most cases, constructing three-dimensional (3D) graphene networks is widely utilized to promote the permeation of electrolyte and enhance the utilization of active materials. In this work, conventional freeze-drying process is utilized in the fabrication of G-MSCs to constitute 3D interconnected networks micro-electrodes, and further by regulating the composition of inks, carbon spheres (CSs) at different mass loadings are introduced into the graphene scaffolds to further increase the active sites of the micro-electrodes. The fabricated all carbon-based MSC with the optimal mass loading of CSs (0.406 mg cm⁻²) exhibits a high specific areal capacitance of 17.01 mF cm⁻² at the scan rate of 10 mV s⁻¹ and a capacitance retention of 93.14% after 10000 cycles at the scan rate of 500 mV s⁻¹. The proposed microfabrication process is facile and fully compatible with modern microtechnologies and will be highly suitable for large-scale production and integration.

© 2018 The Chinese Ceramic Society. Production and hosting by Elsevier B.V. This is an open access article under the CC BY-NC-ND license (<http://creativecommons.org/licenses/by-nc-nd/4.0/>).

1. Introduction

The development of portable, wearable and implantable electronic equipments has generated an immense demand for micro energy storage devices (MESDs) with light weight and high efficiency, which are essential for future energy component in micro/nanorobotics and microelectromechanical systems (MEMSs) [1–8]. Among MESDs, micro-supercapacitors (MSCs) own longer cycle life, higher power density and preferable safety compared with thin-film batteries and micro-batteries, showing great potential in energy storage [1,6]. The traditional processes for fabricating MSCs

include laser scribing [3,9–11], chemical vapor deposition (CVD) [12], electrochemical deposition [13,14], ink-jet printing [15–17], three-dimensional (3D) printing [18,19], injecting [20,21], carbide pyrolysis [22,23] etc. Among which, liquid-based processes including ink-jet printing and injecting have drawn extensive attentions recently since they are easy to be conducted and have the access to large-scale production.

As one of the most significant two-dimensional (2D) carbon materials, graphene has been widely applied in carbon-based MSCs (C-MSCs) due to its excellent electrical conductivity, high stability, high surface area and lack of solid-state diffusion [24–28]. Benefiting from its superb dispersibility, graphene-based materials have been widely studied in ink-jet printing [15,16] and injecting [20] processes with the aim of making graphene into special inks to facilitate the micro-patterning of electrode materials [29–31]. For example, Hyun et al. mixed graphene/ethyl cellulose stabilizer into a solvent system of cyclohexanone/terpineol/di (ethylene glycol) methyl ether by bath sonication [20]. Liu et al. dispersed

* Corresponding author. State Key Laboratory of Advanced Technology for Materials Synthesis and Processing, International School of Materials Science and Engineering, Wuhan University of Technology, Wuhan, 430070, China.

** corresponding author.

E-mail addresses: hel@whut.edu.cn (L. He), mlq518@whut.edu.cn (L. Mai).

Peer review under responsibility of The Chinese Ceramic Society.

electrochemically exfoliated graphite/PEDOT into isopropanol (IPA) to prepare stable graphene-based inks [16]. However, the restacking of graphene after natural drying immensely limits the permeation of electrolyte ions, leading to a low loading utilization [28]. Although some efforts are focusing on constructing graphene-based electrodes with unique structure [32–36], relevant techniques of configuring 3D micro-electrodes for ink-derived MSC are still rarely reported.

In this work, graphene oxide (GO) aqueous dispersion is utilized to prepare graphene-based inks, which makes it possible to conduct freeze-drying process based on ice molding mechanism [19,37] and construct 3D conductive graphene-based networks. After freeze-drying, the reduced GO (rGO)-based micro-electrode is transformed from 2D (specific capacitance: 0.26 mF cm^{-2}) into 3D (specific capacitance: 1.17 mF cm^{-2}). The latter one exhibits a higher specific mass capacitance (187.2 F g^{-1}) compared with 2D micro-electrode (41.6 F g^{-1}), which declares the deeper permeation of electrolyte ions benefiting from the 3D structure of the micro-electrode. In addition, due to the excellent solvent property of GO aqueous dispersion [38], carbon spheres (CSs) are easy to be introduced into the inks to further increase the active sites of the final micro-electrodes. By simply regulating the concentration of CSs in the pristine inks, the mass loadings of CSs in micro-electrodes are amenable to be controlled. Finally, MSCs with different mass loadings of CSs were fabricated, demonstrating that MSC with the highest mass loading of CSs (0.406 mg cm^{-2}) possesses the highest specific areal capacitance (17.01 mF cm^{-2}). The environmentally friendly deionized (DI) water is employed as solvent of this kind of inks, which can benefit the formation of 3D networks by freeze-drying process to increase the surface area of the micro-electrodes and facilitate the permeation of electrolyte ions. Our work proposes a promising approach for improving electrochemical performance of MSCs derived from graphene-based inks. In addition, benefiting from the highly controllable process, it is amenable to achieve automatic large-scale production, and by rationally designing the mask, high integration can be achieved.

2. Experimental

2.1. Preparation of GO/CSs dispersion

The CSs were synthesized according to a previous work [39]. 3-aminophenol (0.50 g) and HMTA ($\text{C}_6\text{H}_{12}\text{N}_4$) (2.56 g) were dissolved in 20 mL DI water and stirred for 30 min to obtain a clarified solution. Then, the solution was reserved in a water bath at 85°C with stirring for 24 h. Afterwards, centrifugation was conducted to separate the particles followed by washing with DI water for 4 times and then vacuum dried at 80°C overnight. After the particles were carbonized at 800°C for 5 h under a flowing gas of $\text{H}_2\text{O}/\text{N}_2$ (heating rate: 2°C min^{-1}), the CSs with uniform diameter were finally obtained. To fabricate micro-electrodes with different mass loadings of CSs, the inks with different ratios of GO/CSs were prepared in advance. Firstly, 9, 18 and 27 mg CSs were respectively added into 1 mL GO dispersion (3 mg mL^{-1}) (see Supporting Information for preparation details) to obtain different mass ratios of GO/CSs (1:3, 1:6, 1:9). The mixtures were then treated by ultrasonication and continuous stirring for 10 min and repeated for 4 times to disperse the CSs and a uniform dispersion was obtained.

2.2. Preparation of Au/SU-8 mold

Firstly, a $500 \mu\text{m}$ thick silicon wafer (with 500 nm thick SiO_2 layer) was cut into pieces ($1.2 \text{ cm} \times 1.5 \text{ cm}$), which were then washed by IPA for 15 min and treated by O_2 plasma to make the surface hydrophilic and attachable. Then, a layer of PR1-9000A

photoresist was spin-coated (speed: 4000 rpm , $6\text{--}7 \mu\text{m}$ thick layer) on Si/SiO_2 substrate and micropatterned by photolithography (detailed size is shown in Fig. S1, the total area is 0.097 cm^2). Afterwards, Cr/Au layers ($5/100 \text{ nm}$) were deposited on the sample by physical vapor deposition (PVD), followed by lift-off process employing acetone. After O_2 plasma treatment, a fine micropatterned interdigital Au current collector was obtained, which is shown in Fig. 1a. To obtain the Au/SU-8 mold, SU-8 50 photoresist was spin-coated (speed: 1000 rpm , about $180 \mu\text{m}$ thick) on the surface of Au current collector, followed by aligned photolithography to construct $180 \mu\text{m}$ width SU-8 walls and Au/SU-8 molds were finally obtained (Fig. 1b).

2.3. Microfabrication of rGO/CSs-MSCs

The Au/SU-8 molds were then treated by O_2 plasma (150 W , 5 min) to make the surface hydrophilic and inks with different mass ratios of GO/CSs (1:3, 1:6, 1:9) were injected into the molds ($1.8 \mu\text{L}$ ink for each micro-electrode). It should be emphasized that the ink with higher CSs concentration (more than 27 mg mL^{-1}) is difficult to be injected into the molds. Rapidly, the sample was transferred into the refrigerator (-40°C) to freeze the dispersion in seconds in order to avoid the evaporation. After gelation, the sample was transferred into a special equipment (surrounded by ice cube to maintain low temperature) to ensure the effect of freeze-drying. After freeze-drying for 3 days, GO/CSs based micropatterns with 3D structure were obtained. Afterwards, the samples were annealed at 300°C for 1 h (heating rate: 1°C min^{-1}), as the SU-8 structure is still stable (insulated) and GO was transformed into rGO, after coated by H_2SO_4 -PVA electrolyte, rGO/CSs-MSCs (denoted as $\text{rGO}_1/\text{CSs}_3$ -MSC, $\text{rGO}_1/\text{CSs}_6$ -MSC and $\text{rGO}_1/\text{CSs}_9$ -MSC, respectively) were finally fabricated. In order to probe the effects of

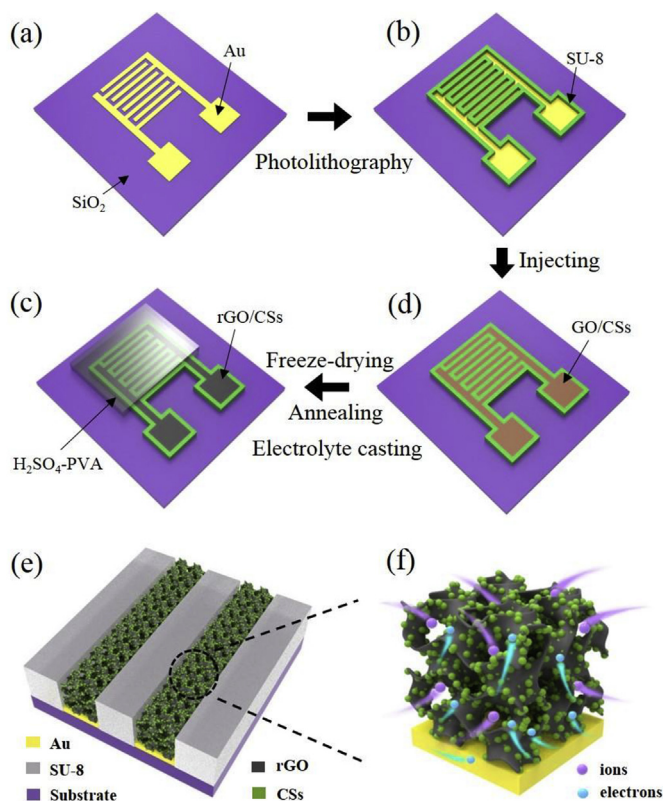


Fig. 1. Schematic illustration of a-d) the microfabrication process of rGO/CSs-MSC, e) cross section of the micro-electrode and f) electrons/ions transport mechanism.

freeze-drying process and contribution of CSs, 3D-rGO-MSC (pure graphene after freeze-drying) and 2D-rGO-MSC (pure graphene after natural drying) were also fabricated.

2.4. Characterizations of the MSCs

The contact angles were measured by a microscopic contact angle meter (JC2000C, Powereach). The morphologies were observed by field-emission scanning electron microscopy (SEM, JEOL-7100F) and transmission electron microscopy (TEM, Titan G2 60-300 Probe Cs Corrector HRSTEM). The surface composition was investigated by X-ray photoelectron spectroscopy (XPS, VG MultiLab 2000). Raman spectrum was recorded using a LabRAM HR Evolution & Smart SPM. The nitrogen adsorption-desorption isotherms were measured by Tristar-3020 instrument at 77 K. The electrochemical tests (utilizing two electrodes system) were conducted by an Autolab (PGSTAT302N).

2.5. Electrochemical measurements

All of the electrochemical measurements were conducted using a two-electrodes system employing H₂SO₄-PVA electrolyte. The electrochemical calculation was according to the previous work [40]. The cyclic voltammetry (CV) tests and galvanostatic charge-discharge (GCD) tests were delivered at the potential window from 0 to 1 V and electrochemical impedance spectroscopy (EIS) tests were conducted at the frequency from 0.01 to 500000 Hz. The specific areal capacitance was calculated from the CV curves, according to the following equation:

$$C_{area} = \frac{\int I(V)dU}{2 \times s \times U} \quad (1)$$

in which $\int I(V)dU$ is the mathematic area of the CV curves, and s (V s⁻¹) refers to the scan rate. U (V) is the potential window. To calculate energy density and power density, the following equations were used:

$$E_{area} = \frac{C_{area} \times U^2}{7200} \quad (2)$$

$$P_{area} = \frac{E_{area}}{\Delta t} \times 3600 \quad (3)$$

where C_{area} (mF cm⁻²) is the specific areal capacitance, and U (V) is the potential window. Δt (s) is the discharge time. The internal resistance was calculated from the IR drop according to the following equation:

$$R = \frac{\Delta V}{2 \times I \times A} \quad (4)$$

in which ΔV (V) is the drop potential during the GCD tests, and I (mA cm⁻²) is the current density utilized in the GCD tests. A (cm²) is the area of the micro-electrodes. The coulombic efficiency was calculated using the following equation:

$$\eta = \frac{T_D}{T_C} \quad (5)$$

where T_D (s) and T_C (s) represent the discharge time and charge time, respectively.

3. Results and discussion

3.1. Microfabrication process of MSCs

The CSs were synthesized by previously reported method [39]. The SEM images of the CSs before and after carbonization are shown in Fig. S2. After carbonization, the volume of CSs shrinks by ~10% and the CSs exhibit average diameter around 1 μm. To investigate the effect of H₂O activation during annealing, the nitrogen-adsorption-desorption measurements for CSs annealed in N₂/H₂O and N₂ were conducted, shown in Fig. S3. The CSs with H₂O activation exhibit an improved BET surface area from 287.7 to 478.9 m² g⁻¹. These two samples both have relatively centralized pore size distribution ranging from 1.8 to 3.8 nm, shown in Figs. S3b and d. For the preparation of homogenous GO/CSs-based inks, CSs were added into 3 mg mL⁻¹ GO dispersion to obtain GO/CSs-based inks with different concentrations of CSs. The mass ratios of GO/CSs were controlled to be 1:3, 1:6 and 1:9, therefore the concentrations of CSs were determined to be 9, 18 and 27 mg mL⁻¹. After sufficient stirring and sonication, the CSs were uniformly dispersed into the GO suspension and stable inks were obtained (Fig. S4).

The Au/SU-8 molds were fabricated using photolithography, as shown in Fig. 1a, b. Firstly, the micro-patterning of PR1-9000A photoresist (Futurrex, Inc. Co., Ltd) was conducted on a Si/SiO₂ wafer by photolithography, followed by Au deposition using PVD. After the lift-off process by acetone, Au micropatterns were obtained (Fig. 1a). Then, SU-8 50 photoresist (NIPPON KAYAKU, Co., Ltd) was spin-coated on the sample and aligned photolithography was conducted to prepare SU-8 walls (Fig. 1b). The obtained Au/SU-8 molds were treated by O₂ plasma to obtain hydrophilic surface. The contact angle test results (using GO dispersion) are shown in Fig. S5, indicating that the hydrophilia of SU-8 layer is improved by O₂ plasma treatment (almost no effect on Au layer), which will facilitate the injecting process. Afterwards, the inks were injected into the molds, which were then frozen in seconds at -40 °C. When the GO/CSs-based interdigital micropatterns were frozen, the solid portion (GO/CSs) was forced to align along the boundaries of ice crystals. The 3D networks gradually formed by crosslinking between GO sheets through π-π interactions [18,27]. During the freeze-drying process, the ice sublimated from the pores and 3D GO/CSs aerogel was obtained. Finally, the sample was annealed to transform GO into rGO, and the rGO/CSs-based MSC was fabricated (Fig. 1c).

The process and corresponding optical microscope images are shown in Fig. S6, demonstrating the uniform micropatterns and the high feasibility of the process. The widths of the fingers and gaps are approximately 180 μm. Fig. 1e is the schematic illustration of the cross section of the micro-electrode. Au layer and rGO/CSs networks on Si/SiO₂ are supported by SU-8 molds, possessing a positive effect on the mechanical stability of the MSC. Fig. 1f presents the mechanism of ions/electrons transportation: the rGO aerogel serves as 3D conductive networks and the porous structure is certain to obtain excellent ions permeation and diffusion kinetics; CSs are uniformly dispersed in rGO networks, leading to the increase of active sites for reversible adsorption/desorption of electrolyte ions. With the existence of SU-8 walls, the direct transport of ions between fingers will be hindered [41,42], however, due to the porous microelectrodes, during charge and discharge, electrolyte ions can pass through the porous microelectrode in the vertical direction and migrate over the SU-8 walls from one finger to another finger. In addition, with the bottom Au layer acting as the current collector for electron transport, the whole MSC is highly promising to exhibit a relatively low internal resistance. The finally fabricated MSCs derived from inks with the ratio of GO/CSs at 1:3, 1:6 and 1:9 are named as rGO₁/CSs₃-MSC, rGO₁/CSs₆-MSC and

rGO₁/CSs₉-MSC, respectively. To investigate the effect of freeze-drying process, naturally dried and freeze-dried MSCs derived from pure GO ink (denoted as 2D-rGO-MSC and 3D-rGO-MSC, respectively) are also fabricated.

3.2. Improvement of electrochemical performance for MSCs

The morphologies of 2D-rGO-MSC and 3D-rGO-MSC were compared to accurately reveal the effect of freeze-drying process, which are shown in Figs. S7a and b. As indicated in Fig. S7a, the graphene stacks together and forms a smooth surface, whereas the graphene shown in Fig. S7b interconnects in three dimension and forms cross-linked conductive networks. It is definite that the 3D structure could obtain higher specific surface area, which will lead to a higher capacitance and more efficient ion diffusion. Calculated from the CV curves (Fig. S7c), the specific areal capacitances of 2D-rGO-MSC and 3D-rGO-MSC are 0.26 mF cm⁻² and 1.17 mF cm⁻², respectively. Since the concentration of GO in the pristine inks and injecting amount are facial to control, the areal mass loading of GO (M_{area}) can be calculated according to the following equation:

$$M_{area} = \frac{V \times c}{A} \quad (6)$$

where V (mL) is the injecting amount of the inks (1.8 μL for each micro-electrode), and c (mg mL⁻¹) represents the utilized concentration of GO in the inks (3 mg mL⁻¹). A (cm²) is the foot print area of each micro-electrode (0.120 cm²). The calculated M_{area} of GO in MSCs is 0.045 mg cm⁻². As there is a mass loss after annealing, thermogravimetric (TG) analysis test was conducted to determine the mass retention at 300 °C (Fig. S8), and a mass retention of 56.17% was obtained after the reduction of GO. So the M_{area} of rGO was calculated (0.045 mg cm⁻² × 56.17%) to be 0.025 mg cm⁻². The specific mass capacitance of graphene exhibiting in 2D-rGO-MSC and 3D-rGO-MSC can be calculated from the following equation [43].

$$C_{mass} = \frac{4 \times C_{area}}{M_{area}} \quad (7)$$

where C_{area} (mF cm⁻²) represents the specific areal capacitance, of which, 2D-rGO-MSC and 3D-rGO-MSC are 0.26 and 1.17 mF cm⁻², respectively. M_{area} (mg cm⁻²) refers to the areal mass loading, both 2D-rGO-MSC and 3D-rGO-MSC are 0.025 mg cm⁻². Therefore the calculated C_{mass} of graphene in 2D-rGO-MSC and 3D-rGO-MSC are 41.6 and 187.2 F g⁻¹, respectively. The improvement of electrochemical performance can be ascribed to the following reasons: (1) the restacking of graphene is prevented by freeze-drying process and 3D micro-electrode with higher surface area was constructed; (2) the 3D micro-electrode facilitates the permeation of electrolyte ions and allows much more contact area between electrode and electrolyte; (3) the graphene scaffolds possess an interlaced porous structure, which benefits to the diffusion of electrolyte ions during charge/discharge. The C_{mass} of graphene exhibiting in 3D-rGO-MSC (187.2 F g⁻¹) is comparable with the highest level of previously reported works [24], including rGO-cellulose paper (120 F g⁻¹) [25], laser-scribed 3D graphene (265 F g⁻¹) [44], holey graphene frameworks (298 F g⁻¹) [45] and liquid-mediated graphene film (203 F g⁻¹) [46]. The considerable capacitance is due to the high utilization of the active material and abundant oxygen functional groups remaining on the graphene sheets (can provide pseudo-capacitance) after annealing at 300 °C.

In consideration of the intrinsic relatively high electrochemical activity of CSs [39] and their excellent combination with graphene, CSs were introduced to obtain a unique 3D structure and further

increase the active sites of the micro-electrode. MSCs with different mass loadings of CSs (rGO₁/CSs₃-MSC, rGO₁/CSs₆-MSC and rGO₁/CSs₉-MSC, see **Experiment section** for details) were obtained in order to detect the effects of CSs participating in the composite micro-electrodes. As shown in Fig. 2a-f, CSs are uniformly distributed on the surface of graphene sheets, which indicates the superb dispersion of CSs in the pristine inks. The cross sectional SEM images of different MSCs are shown in Fig. S9. In a given space of the fingers, the micro-electrodes with higher mass loading of CSs are more compact, which is promising to achieve higher specific areal capacitance [9]. Furthermore, the CV (at the scan rate of 10 mV s⁻¹) and GCD (at the current density of 0.1 mA cm⁻²) tests results are presented in Fig. 2g, h. With the content of CSs increasing, the response current increases, indicating that the CSs have a significant contribution in capacitance. Calculated from the CV curves in Fig. 2g, the capacitances of rGO₁/CSs₃-MSC, rGO₁/CSs₆-MSC and rGO₁/CSs₉-MSC are 7.39, 9.99 and 17.01 mF cm⁻², respectively. As shown in Fig. 2h, the MSC with a higher mass loading of CSs possesses the longer discharge time (72.5, 101.3 and 173.0 s, respectively), which manifests that, the MSC with increased mass loading of CSs will obtain improved active sites in the micro-electrodes and lead to a higher capacitance. The areal mass loadings of CSs (M_{area}) can be calculated according to equation (6). Where V (mL) for the injecting amount of the inks is 1.8 μL for each micro-electrode, and c (mg mL⁻¹) represents the utilized concentration of CSs in the inks, which are 9, 18 and 27 mg mL⁻¹ for rGO₁/CSs₃-MSC, rGO₁/CSs₆-MSC and rGO₁/CSs₉-MSC, respectively. A (cm²) is the foot print area of each microelectrode (0.120 cm²). The calculated areal mass loadings of CSs in MSCs are 0.135, 0.271 and 0.406 mg cm⁻², respectively. Calculated from C_{area} and M_{area} according to equation (7), the C_{mass} of CSs exhibiting in rGO₁/CSs₃-MSC, rGO₁/CSs₆-MSC and rGO₁/CSs₉-MSC are respectively 184.30, 130.18 and 156.06 F g⁻¹ (minus the capacitance contribution of rGO), which is comparable with the result in reference work (282 F g⁻¹) [39]. The approximation is ascribed to the superior architecture of the interdigital devices and excellent permeation of electrolyte resulting from the 3D structure of the micro-electrodes and utilization of H₂SO₄-PVA electrolyte. The corresponding specific areal capacitances are plotted in Fig. 2i (at the scan rate of 10 mV s⁻¹), it is apparent that the capacitance of the MSC increases as mass loading of CSs increases. That can be ascribed to this reason: the high-surface-area CSs provide abundant active sites for adsorption/desorption of electrolyte ions, and while mass loading of CSs increases, the active sites increase simultaneously, therefore the MSC with higher mass loading of CSs exhibits improved capability. Since inks with higher concentration of CSs exhibit higher viscosity, it is extremely tough to make the inks flow into the Au/SU-8 molds when the concentration of CSs is more than 27 mg mL⁻¹, therefore the mass loading of CSs at 0.406 mg cm⁻² is the highest level which can be obtained in this work.

The EIS curves (range from 500 kHz to 0.01 Hz) of 2D-rGO-MSC, 3D-rGO-MSC, rGO₁/CSs₃-MSC, rGO₁/CSs₆-MSC and rGO₁/CSs₉-MSC are shown in Figs. S10a and b. Judging from the high frequency region, these five MSCs exhibit comparable equivalent series resistance (ESR), which suggests that the introduction of CSs has no obvious impact on the ESR. By comparing the low frequency region, the slopes of freeze-dried MSCs are much higher than that of naturally dried MSC, indicating their faster ions diffusion, which owes to the 3D structure of their micro-electrodes [7,47–49]. The diffusion coefficient D of ions in the porous electrode can be calculated according to the supplementary equation (1, 2) [50,51]. The linear fitting between Z' and $\omega^{-1/2}$ (ω is frequency) is shown in Figs. S10c and d and the slope in the fitting line represents σ . The slope value of 2D-rGO-MSC ($k_1 = 24671$) is much higher than others, indicating its poor diffusion kinetics resulting from the restacking of

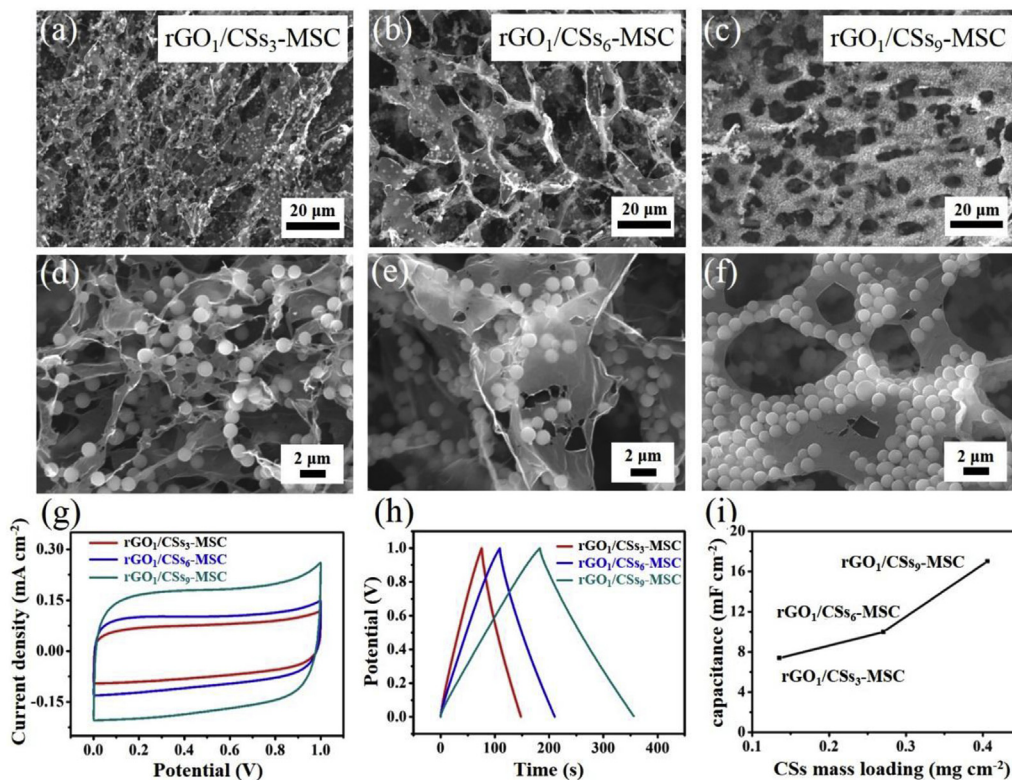


Fig. 2. SEM images of a, d) rGO_1/CS_{S_3} -MSC, b, e) rGO_1/CS_{S_6} -MSC and c, f) rGO_1/CS_{S_9} -MSC. g) CV curves of rGO_1/CS_{S_3} -MSC, rGO_1/CS_{S_6} -MSC and rGO_1/CS_{S_9} -MSC at the scan rate of 10 mV s^{-1} with a potential window from 0 to 1 V. h) GCD curves of rGO_1/CS_{S_3} -MSC, rGO_1/CS_{S_6} -MSC and rGO_1/CS_{S_9} -MSC at the current density of 0.1 mA cm^{-2} with a potential window from 0 to 1 V. i) Specific capacitances of MSCs with different mass loadings of CSs.

graphene. Among the freeze-dried MSCs, the slope values of rGO_1/CS_{S_3} -MSC ($k_3 = 452$), rGO_1/CS_{S_6} -MSC ($k_4 = 106$) and rGO_1/CS_{S_9} -MSC ($k_5 = 181$) are lower than that of 3D- rGO -MSC ($k_2 = 2018$), which indicates that the CSs imbed into the graphene pieces, and further restrain the restacking of graphene and provide more efficient path for the migration of electrolyte ions.

3.3. Characterization of rGO_1/CS_{S_9} -MSC and further application

The digital camera image of rGO_1/CS_{S_9} -MSC is shown in Fig. 3a. The scale of whole MSC is comparable with the human's finger, which will be suitable for applications in implantable or wearable devices. Fig. 3b is the cross-sectional SEM image of rGO_1/CS_{S_9} -MSC, it can be observed that the SU-8 micropatterns on Si/SiO₂ wafer possess an average height of $180\text{ }\mu\text{m}$, which will ensure a high mass loading of the active materials. As shown in the high magnification cross-sectional SEM images (Fig. 3c and inset image), it is obvious that the uniformly distributed CSs and rGO aerogel interconnect into 3D networks, forming a unique porous micro-electrode. Fig. 3d, e are low and high magnification SEM images of the top surface, also indicating its porous characteristic. Due to the volumetric shrinkage of SU-8 photoresist after annealing, some cracks are observed. With the existence of Au current collector, the cracks have no effect on the electron transport. Fig. 3f is the TEM image of rGO_1/CS_{S_9} -MSC, it is apparent that the CS (amorphous part) is half covered by rGO (graphite part), among which, the covered area is conducive to the migration of electrons (from rGO to CSs) and uncovered area will be of benefit to the permeation of electrolyte ions. To investigate the inherent properties, rGO_1/CS_{S_9} micro-electrode was characterized by Raman spectroscopy, XPS and nitrogen adsorption-desorption

measurements. As presented in Fig. 3g, the Raman spectrum of rGO_1/CS_{S_9} micro-electrode exhibits a D band ($\approx 1340\text{ cm}^{-1}$) together with a relatively narrow G band ($\approx 1585\text{ cm}^{-1}$), which correspond with disordered carbon/defective graphitic structure and graphitic sp^2 -bonded carbon, respectively [39]. The sample demonstrates a comparable and relatively high I_D/I_G ratio (1.14), indicating the amorphous form of carbon [39]. To investigate the surface composition of rGO_1/CS_{S_9} micro-electrode, the XPS measurement was conducted (Fig. 3h, i and Fig. S11). As shown in the inset image of Fig. 3h, the contents of carbon, nitrogen and oxygen are respectively 81.63%, 3.22% and 15.14%. Originated from CSs (nitrogen-doped), nitrogen (Fig. 3i) can be divided into four types: pyridinic N located at 398.2 eV (15.33%), pyrrolic N at 400.6 eV (49.43%), quaternary N at 401.4 eV (3.13%), and pyridine N–O moieties at 405.2 eV (32.11%) [39]. According to previous reports [39,52–54], the negatively charged groups pyridinic N and pyrrolic N are located at the edges of the carbons, which contribute to the pseudocapacitance, and the positively charged quaternary N and pyridine N–O moieties help electron transport in carbon. Nitrogen adsorption-desorption isotherms are demonstrated in Fig. S12, indicating its microporous structure. The Brunner-Emmet-Teller (BET) surface area, micropore surface area and micropore volume are determined to be $402.88\text{ m}^2\text{ g}^{-1}$, $362.43\text{ m}^2\text{ g}^{-1}$ and $0.18\text{ cm}^3\text{ g}^{-1}$, respectively.

To investigate the electrochemical performance of rGO_1/CS_{S_9} -MSC, CV test was conducted at various scan rates varying from 10 to 100 mV s^{-1} (Fig. 4a) and GCD test was conducted at different current densities from 0.1 to 1 mA cm^{-2} (Fig. S13). It is obvious that, all of the CV curves in Fig. 4a are rectangular and with the scan rate increasing, the response current increases with the same multiple, which further indicates the efficient diffusion of electrolyte ions in

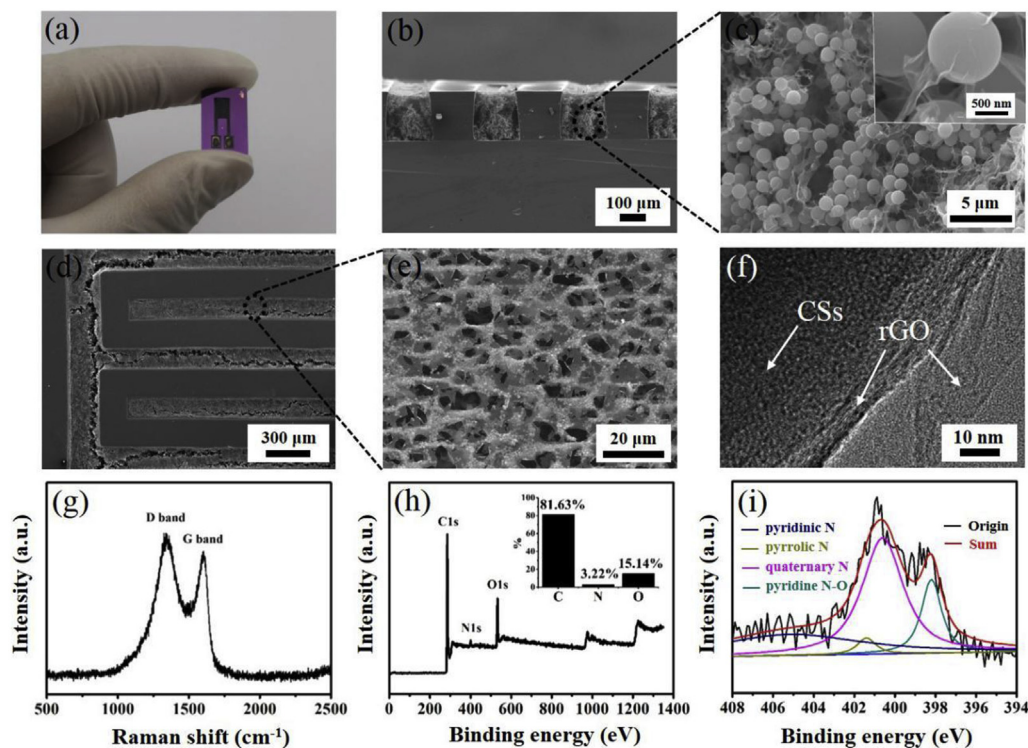


Fig. 3. a) Digital camera image of rGO₁/CSs₉-MSC. b, c) Cross sectional SEM images of rGO₁/CSs₉-MSC. d, e) Top surface SEM images of rGO₁/CSs₉-MSC. f) TEM image of rGO₁/CSs₉-MSC. g, h, i) Raman spectrum, XPS spectrum (the inset image shows the content of C, N and O) and high-resolution N 1s spectrum of rGO₁/CSs₉-MSC.

the micro-electrode of rGO₁/CSs₉-MSC. The GCD curves in Fig. S13 display relatively symmetric triangular shapes. At the current density of 0.1 mA cm⁻², the rGO₁/CSs₉-MSC exhibits excellent coulombic efficiency (94.54%), and the internal resistance calculated from the IR drop is 0.975 Ω. The low internal resistance is benefited from the existence of current collector (Au layer) and graphene networks: the Au layer serves the function of highway for planar electron transport and the graphene networks serve as the 3D conductive framework. Calculated from the CV curves, the specific areal capacitances of rGO₁/CSs₉-MSC under different scan rates are shown in Fig. S14, which shows excellent rate performance. At the scan rate of 10 mV s⁻¹, the rGO₁/CSs₉-MSC exhibits a high specific capacitance of 17.01 mF cm⁻², which exceeds many reported naturally dried graphene-based MSCs (5 mF cm⁻²) [16], scalable fabricated MSCs (0.7 mF cm⁻²) [15] and scalable, self-aligned printed MSCs (0.268 mF cm⁻²) [20], indicating the significant effect of freeze-drying process and loading of CSs. At the scan rate of 500 mV s⁻¹, the rGO₁/CSs₉-MSC exhibits 93.1% capacitance retention even after 10000 cycles, showing excellent cycling performance (Fig. 4b). Calculated from CV curves, at the scan rate of 10 mV s⁻¹, the rGO₁/CSs₉-MSC exhibits an energy density of 0.13 mWh cm⁻² and a power density of 4.72 mW cm⁻². Results of energy density and power density (calculated from different scan rates) are listed in the Ragone plots (Fig. 4c), which are comparable with graphene/phosphorene hybrid films [55] and vertically aligned graphene [56], and higher than those of graphene-based in-plan MSC [7], cellular graphene-based MSC [57], hydrated GO-based MSC [3], rGO-based monolithic MSC [58] and sulfur-doped graphene-based MSC [59].

In most cases, because of their wider voltage windows or higher capacitance, connecting several MSCs in series, parallel or mixed combination are more applicable than single MSC employed in integrated circuits [14,15]. In our work, several MSCs are connected in series (denoted as 2S, 3S, 4S), parallel (denoted as 2P, 4P) and mixed combination (denoted as 2P × 2S), the connection types and their electrochemical test results are shown in Fig. 4d-i. As shown in Fig. 4d, g, the voltages of 2S, 3S, 4S can reach 2 V, 3 V, 4 V, respectively and their capacitances deliver 1/2, 1/3, 1/4 times as that of single MSC. When the voltage reaches 2 V, the “bank” can power a LED successfully, which is shown in the inset image of Fig. 4b. When connected in 2P and 4P, the capacitances are respectively 2 and 4 times as that of single MSC while the voltage remains the same, which are demonstrated in Fig. 4e, h. To increase both the voltage and capacitance, every two MSCs are connected in series and then connected in parallel to form the mixed combination (2P × 2S). Benefiting from this design, the capacitance of this combined MSC is increased by 2 times and so does the operating voltage window, which is apparent in Fig. 4f, i.

4. Conclusions

In summary, the rGO aerogel-based MSC is fabricated by injecting and freeze-drying processes using environmentally friendly aqueous GO-based inks. Benefiting from the 3D structure of the microelectrode, the 3D-rGO-MSC exhibits a higher specific mass capacitance (187.2 F g⁻¹) comparing with the 2D-rGO-MSC (41.6 F g⁻¹). With the further introduction of CSs, the MSCs exhibit improved electrochemical performance. When the areal mass loading of CSs reaches 0.406 mg cm⁻², the MSC exhibits a high

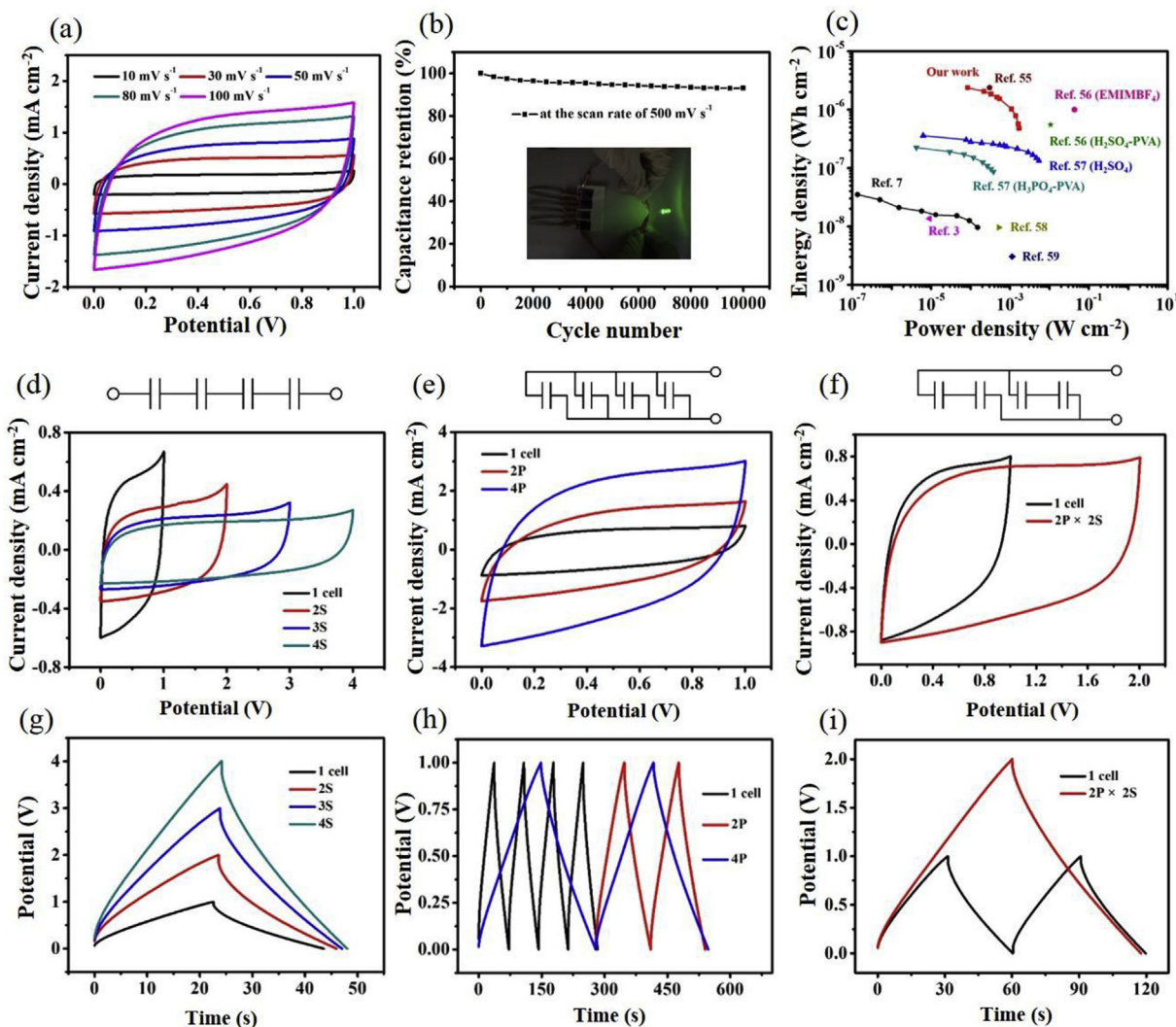


Fig. 4. Electrochemical performances of rGO₁/CS₉-MSC using H₂SO₄-PVA electrolyte. a) CV curves at different scan rates with a potential window from 0 to 1 V b) Cycling performance of rGO₁/CS₉-MSC at the scan rate of 500 mV s⁻¹ after 10000 cycles. Inset image shows a LED powered by four series-connected MSCs. c) Ragone plots of specific areal energy density and power density of rGO₁/CS₉-MSC and other reported MSCs. d-i) Schematic illustration of 4 MSCs connected in series, parallel and mixed combinations. CV curves at the scan rate of 10 mV s⁻¹ and GCD curves at the current density of 0.1 mA cm⁻² for d, g) 1 cell, 2S, 3S, 4S e, h) 1 cell, 2P, 4P and f, i) 1 cell, 2P × 2S.

specific areal capacitance of 17.01 mF cm⁻² at the scan rate of 10 mV s⁻¹, which is ascribed to the sufficient active sites for adsorption/desorption of electrolyte ions provided by CSs. The fabricated rGO₁/CS₉-MSC also has a remarkable long-term cycling performance: with 93.14% capacitance retention after 10,000 cyclic voltammetry cycles. The utilized inks are stable, safe, nontoxic and low-cost, the proposed microfabrication process is facile and controllable, and this novel all carbon-based MSC with 3D micro-electrode exhibits outstanding performance, which will pave the way for future investigation of graphene-based inks applied in high-performance micro-devices/systems.

Conflicts of interest

Authors declare that there are no conflicts of interest.

Acknowledgements

This work was supported by the National Natural Science Fund

for Distinguished Young Scholars (51425204), the National Natural Science Foundation of China (51521001, 51502227, 51579198, 51802239), the National Key Research and Development Program of China (2016YFA0202603, 2016YFA0202604), the Programme of Introducing Talents of Discipline to Universities (B17034), the China Postdoctoral Science Foundation (2015T80845), the Yellow Crane Talent (Science & Technology) Program of Wuhan City, the Wuhan Morning Light Plan of Youth Science and Technology (No. 2017050304010316), the Fundamental Research Funds for the Central Universities (WUT: 2017III005, 2017III009, 2018IVA091) and the Students innovation and entrepreneurship training program (WUT: 20171049701005).

Appendix A. Supplementary data

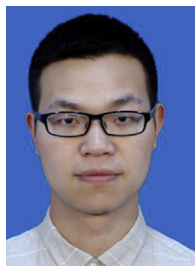
Supplementary data to this article can be found online at <https://doi.org/10.1016/j.jmat.2018.11.009>.

References

- [1] Chmiola J, Largeot C, Taberna PL, Simon P, Gogotsi Y. Monolithic carbide-derived carbon films for micro-supercapacitors. *Science* 2010;328:480–3.
- [2] El-Kady MF, Kaner RB. Scalable fabrication of high-power graphene micro-supercapacitors for flexible and on-chip energy storage. *Nat Commun* 2013;4:1475.
- [3] Gao W, Singh N, Song L, Liu Z, Reddy AL, Ci L, Vajtai R, Zhang Q, Wei B, Ajayan PM. Direct laser writing of micro-supercapacitors on hydrated graphite oxide films. *Nat Nanotechnol* 2011;6:496–500.
- [4] Kyeremateng NA, Brousse T, Pech D. Microsupercapacitors as miniaturized energy-storage components for on-chip electronics. *Nat Nanotechnol* 2017;12:7–15.
- [5] Niu Z, Zhang L, Liu L, Zhu B, Dong H, Chen X. All-solid-state flexible ultrathin micro-supercapacitors based on graphene. *Adv Mater* 2013;25:4035–42.
- [6] Pech D, Brunet M, Durou H, Huang P, Mochalin V, Gogotsi Y, Taberna PL, Simon P. Ultrahigh-power micrometre-sized supercapacitors based on onion-like carbon. *Nat Nanotechnol* 2010;5:651–4.
- [7] Wu ZS, Parvez K, Feng X, Mullen K. Graphene-based in-plane micro-supercapacitors with high power and energy densities. *Nat Commun* 2013;4:2487.
- [8] Liu L, Niu Z, Zhang L, Zhou W, Chen X, Xie S. Nanostructured graphene composite papers for highly flexible and foldable supercapacitors. *Adv Mater* 2014;26:4855–62.
- [9] Jiang Q, Kurra N, Xia C, Alshareef HN. Hybrid microsupercapacitors with vertically scaled 3D current collectors fabricated using a simple cut-and-transfer strategy. *Adv. Energy Mater.* 2017;7:1601257.
- [10] Peng Y-Y, Akuzum B, Kurra N, Zhao M-Q, Alhabeb M, Anasori B, Kumbur EC, Alshareef HN, Ger M-D, Gogotsi Y. All-MXene (2D titanium carbide) solid-state microsupercapacitors for on-chip energy storage. *Energy Environ Sci* 2016;9:2847–54.
- [11] Pu X, Liu M, Li L, Han S, Li X, Jiang C, Du C, Luo J, Hu W, Wang ZL. Wearable textile-based in-plane microsupercapacitors. *Adv. Energy Mater.* 2016;6:1601254.
- [12] Lin J, Zhang C, Yan Z, Zhu Y, Peng Z, Hauge RH, Natelson D, Tour JM. 3-Dimensional graphene carbon nanotube carpet-based microsupercapacitors with high electrochemical performance. *Nano Lett* 2013;13:72–8.
- [13] Liu Z, Tian X, Xu X, He L, Yan M, Han C, Li Y, Yang W, Mai L. Capacitance and voltage matching between MnO₂ nanoflake cathode and Fe₂O₃ nanoparticle anode for high-performance asymmetric micro-supercapacitors. *Nano Res* 2017;10:2471–81.
- [14] Zhu M, Huang Y, Huang Y, Li H, Wang Z, Pei Z, Xue Q, Geng H, Zhi C. A highly durable, transferable, and substrate-versatile high-performance all-polymer micro-supercapacitor with plug-and-play function. *Adv Mater* 2017;29:1605137.
- [15] Li J, Sollami Delektas S, Zhang P, Yang S, Lohe MR, Zhuang X, Feng X, Östling M. Scalable fabrication and integration of graphene microsupercapacitors through full inkjet printing. *ACS Nano* 2017;11:8249–56.
- [16] Liu Z, Wu ZS, Yang S, Dong R, Feng X, Mullen K. Ultraflexible in-plane micro-supercapacitors by direct printing of solution-processable electrochemically exfoliated graphene. *Adv Mater* 2016;28:2217–22.
- [17] Wang S, Liu N, Tao J, Yang C, Liu W, Shi Y, Wang Y, Su J, Li L, Gao Y. Inkjet printing of conductive patterns and supercapacitors using a multi-walled carbon nanotube/Ag nanoparticle based ink. *J Mater Chem* 2015;3:2407–13.
- [18] Chen B, Jiang Y, Tang X, Pan Y, Hu S. Fully packaged carbon nanotube supercapacitors by direct ink writing on flexible substrates. *ACS Appl Mater Interfaces* 2017;9:28433–40.
- [19] Li W, Li Y, Su M, An B, Liu J, Su D, Li L, Li F, Song Y. Printing assembly and structural regulation of graphene towards three-dimensional flexible micro-supercapacitors. *J Mater Chem* 2017;5:16281–8.
- [20] Hyun WJ, Secor EB, Kim C-H, Hersam MC, Francis LF, Frisbie CD. Scalable, self-aligned printing of flexible graphene micro-supercapacitors. *Adv. Energy Mater.* 2017;7:1700285.
- [21] Kim SK, Koo HJ, Lee A, Braun PV. Selective wetting-induced micro-electrode patterning for flexible micro-supercapacitors. *Adv Mater* 2014;26:5108–12.
- [22] Hong X, He L, Ma X, Yang W, Chen Y, Zhang L, Yan H, Li Z, Mai L. Micro-structuring of carbon/tin quantum dots via a novel photolithography and pyrolysis-reduction process. *Nano Res* 2017;10:3743–53.
- [23] Yang W, He L, Tian X, Yan M, Yuan H, Liao X, Meng J, Hao Z, Mai L. Carbon-mems-based alternating stacked MoS₂@rGO-CNT micro-supercapacitor with high capacitance and energy density. *Small* 2017;13:1700639.
- [24] El-Kady MF, Shao Y, Kaner RB. Graphene for batteries, supercapacitors and beyond. *Nat. Rev. Mater* 2016;1:16033.
- [25] Shao Y, El-Kady MF, Wang LJ, Zhang Q, Li Y, Wang H, Mousavi MF, Kaner RB. Graphene-based materials for flexible supercapacitors. *Chem Soc Rev* 2015;44:3639–65.
- [26] Wu Z-S, Feng X, Cheng H-M. Recent advances in graphene-based planar micro-supercapacitors for on-chip energy storage. *Nat. Rev. Mater* 2014;1:277–92.
- [27] Xiong G, Meng C, Reifengerger RG, Irazoqui PP, Fisher TS. A review of graphene-based electrochemical microsupercapacitors. *Electroanalysis* 2014;26:30–51.
- [28] Xia Y, Mathis TS, Zhao MQ, Anasori B, Dang A, Zhou Z, Cho H, Gogotsi Y, Yang S. Thickness-independent capacitance of vertically aligned liquid-crystalline MXenes. *Nature* 2018;557:409–12.
- [29] Liu L, Niu Z, Chen J. Unconventional supercapacitors from nanocarbon-based electrode materials to device configurations. *Chem Soc Rev* 2016;45:4340–63.
- [30] Liu L, Niu Z, Chen J. Design and integration of flexible planar micro-supercapacitors. *Nano Res* 2017;10:1524–44.
- [31] Wang Q, Wang X, Wan F, Chen K, Niu Z, Chen J. An all-freeze-casting strategy to design topographical supercapacitors with integrated architectures. *Small* 2018;14. e1800280.
- [32] Miller JR, Outlaw RA, Holloway BC. Graphene double-layer capacitor with ac line-filtering performance. *Science* 2010;329:1637–9.
- [33] Zhu C, Liu T, Qian F, Han TY, Duoss EB, Kuntz JD, Spadaccini CM, Worsley MA, Li Y. Supercapacitors based on three-dimensional hierarchical graphene aerogels with periodic macropores. *Nano Lett* 2016;16:3448–56.
- [34] Chen J, Bo Z, Lu G. Vertically-oriented graphene. Springer International Publishing; 2015.
- [35] Sun H, Mei L, Liang J, Zhao Z, Lee C, Fei H, Ding M, Lau J, Li M, Wang C. Three-dimensional holey-graphene/niobia composite architectures for ultrahigh-rate energy storage. *Science* 2017;356:599–604.
- [36] Yoon Y, Lee K, Kwon S, Seo S, Yoo H, Kim S, Shin Y, Park Y, Kim D, Choi JY. Vertical alignments of graphene sheets spatially and densely piled for fast ion diffusion in compact supercapacitors. *ACS Nano* 2014;8:4580–90.
- [37] Qiu L, Liu JZ, Chang SL, Wu Y, Li D. Biomimetic superelastic graphene-based cellular monoliths. *Nat Commun* 2012;3:1241.
- [38] Raccichini R, Varzi A, Passerini S, Scrosati B. The role of graphene for electrochemical energy storage. *Nat Mater* 2015;14:271–9.
- [39] Yu Q, Guan D, Zhuang Z, Li J, Shi C, Luo W, Zhou L, Zhao D, Mai L. Mass production of monodisperse carbon microspheres with size-dependent supercapacitor performance via aqueous self-catalyzed polymerization. *Chempluschem* 2017;82:1–8.
- [40] Tian X, Shi M, Xu X, Yan M, Xu L, Minhas-Khan A, Han C, He L, Mai L. Arbitrary shape engineerable spiral micropseudocapacitors with ultrahigh energy and power densities. *Adv Mater* 2015;27:7476–82.
- [41] Zheng S, Ma J, Wu Z-S, Zhou F, He Y-B, Kang F, Cheng H-M, Bao X. All-solid-state flexible planar lithium ion micro-capacitors. *Energy Environ Sci* 2018;11:2001–9.
- [42] Zhou F, Huang H, Xiao C, Zheng S, Shi X, Qin J, Fu Q, Bao X, Feng X, Mullen K, Wu ZS. Electrochemically scalable production of fluorine-modified graphene for flexible and high-energy ionogel-based microsupercapacitors. *J Am Chem Soc* 2018;140:8198–205.
- [43] Winter M, Brodd RJ. What are batteries, fuel cells, and supercapacitors? *Chem Rev* 2004;35:4245.
- [44] El-Kady MF, Strong V, Dubin S, Kaner RB. Laser scribing of high-performance and flexible graphene-based electrochemical capacitors. *Science* 2012;335:1326–30.
- [45] Xu Y, Lin Z, Zhong X, Huang X, Weiss NO, Huang Y, Duan X. Holey graphene frameworks for highly efficient capacitive energy storage. *Nat Commun* 2014;5:4554.
- [46] Yang X, Cheng C, Wang Y, Qiu L, Li D. Liquid-mediated dense integration of graphene materials for compact capacitive energy storage. *Science* 2013;341:534–7.
- [47] Wu ZS, Liu Z, Parvez K, Feng X, Mullen K. Ultrathin printable graphene supercapacitors with AC line-filtering performance. *Adv Mater* 2015;27:3669–75.
- [48] Wu ZS, Parvez K, Li S, Yang S, Liu Z, Liu S, Feng X, Mullen K. Alternating stacked graphene-conducting polymer compact films with ultrahigh areal and volumetric capacitances for high-energy micro-supercapacitors. *Adv Mater* 2015;27:4054–61.
- [49] Wu ZS, Parvez K, Winter A, Vieker H, Liu X, Han S, Turchanin A, Feng X, Mullen K. Layer-by-layer assembled heteroatom-doped graphene films with ultrahigh volumetric capacitance and rate capability for micro-supercapacitors. *Adv Mater* 2014;26:4552–8.
- [50] Tang C, Liu Y, Xu C, Zhu J, Wei X, Zhou L, He L, Yang W, Mai L. Ultrafine nickel-nanoparticle-enabled SiO₂ hierarchical hollow spheres for high-performance lithium storage. *Adv Funct Mater* 2018;28:1704561.
- [51] Zhao Y, Feng J, Liu X, Wang F, Wang L, Shi C, Huang L, Feng X, Chen X, Xu L. Self-adaptive strain-relaxation optimization for high-energy lithium storage material through crumpling of graphene. *Nat Commun* 2014;5:4565.
- [52] Deng Y, Xie Y, Zou K, Ji X. Review on recent advances in nitrogen-doped carbons: preparations and applications in supercapacitors. *J Mater Chem* 2016;4:1144–73.
- [53] Wang Q, Yan J, Fan Z. Carbon materials for high volumetric performance supercapacitors: design, progress, challenges and opportunities. *Energy Environ Sci* 2016;9:729–62.
- [54] Wickramaratne NP, Xu J, Wang M, Zhu L, Dai L, Jaroniec M. Nitrogen enriched porous carbon spheres: attractive materials for supercapacitor electrodes and CO₂ adsorption. *Chem Mater* 2014;26:2820–8.
- [55] Xiao H, Wu ZS, Chen L, Zhou F, Zheng S, Ren W, Cheng HM, Bao X. One-step device fabrication of phosphorene and graphene interdigital micro-supercapacitors with high energy density. *ACS Nano* 2017;11:7284–92.
- [56] Zheng S, Li Z, Wu ZS, Dong Y, Zhou F, Wang S, Fu Q, Sun C, Guo L, Bao X. High packing density unidirectional arrays of vertically aligned graphene with enhanced areal capacitance for high-power micro-supercapacitors. *ACS Nano* 2017;11:4009–16.
- [57] Shao Y, Li J, Li Y, Wang H, Zhang Q, Kaner RB. Flexible quasi-solid-state planar micro-supercapacitor based on cellular graphene films. *Mater. Horiz.* 2017;4:

1145–50.

- [58] Wang S, Wu ZS, Zheng S, Zhou F, Sun C, Cheng HM, Bao X. Scalable fabrication of photochemically reduced graphene-based monolithic micro-supercapacitors with superior energy and power densities. *ACS Nano* 2017;11:4283–91.
- [59] Wu ZS, Tan YZ, Zheng S, Wang S, Parvez K, Qin J, Shi X, Sun C, Bao X, Feng X, Mullen K. Bottom-up fabrication of sulfur-doped graphene films derived from sulfur-annulated nanographene for ultrahigh volumetric capacitance micro-supercapacitors. *J Am Chem Soc* 2017;139:4506–12.



Yiming Chen received his Bachelor's degree in Department of Materials Science and Engineering from Wuhan University of Technology (WUT) in 2017. He is currently working toward the Ph.D. degree and his current research focuses on the energy storage materials and devices.



Minghao Guo is an undergraduate in Department of Materials Science and Engineering from Wuhan University of Technology. He's working toward the Bachelor's degree and his current research focuses on the energy storage materials and device.



Liang He is an associate professor of the State Key Laboratory of Advanced Technology for Materials Synthesis and Processing at Wuhan University of Technology. He received his Ph.D. degree from Tohoku University (Japan) in 2013. His current research interests include the micro-fabrication and characterizations of micro/nanostructures and devices for applications in MEMS (Micro Electro Mechanical Systems).



Wei Yang received his Master's degree in Materials Engineering from Wuhan University of Technology in 2017. He is currently a research assistant at Wuhan University of Technology. His research interests focus on developing functional materials for micro energy storage devices.



Lin Xu received his Ph.D. degree in 2013 from School of Materials Science and Engineering at Wuhan University of Technology under the supervision of Professor Liqiang Mai, Professor Qingjie Zhang, and Professor Charles M. Lieber. He was a visiting graduate student (2011–2013) and postdoctoral research fellow (2013–2016) in Lieber Research Group at Harvard University. He is currently a professor at State Key Laboratory of Advanced Technology for Materials Synthesis and Processing, Wuhan University of Technology. His research focuses on nanomaterials and devices for energy storage and conversion.



Jiashen Meng received his B.S. degree from Wuhan University of Technology in 2015. He is currently working toward the Ph.D. degree in Wuhan University of Technology and his current research focuses on the energy conversion and storage materials.



Xiaocong Tian received his Ph.D. degree in materials science and engineering in 2016 from Wuhan University of Technology under the supervision of Prof. Liqiang Mai. Afterward, he worked as a postdoctoral research fellow working with Prof. Kun Zhou at the Singapore Centre for 3D Printing, Nanyang Technological University, Singapore. He is currently an associate professor at China University of Geosciences. His research interests include 3D printing, novel nanomaterials, and energy-related devices.



Xinyu Ma received his B.S. degree from Wuhan University of Technology in 2014, and he is now a Ph.D. candidate in Wuhan University of Technology. His current research focuses on the energy storage materials and devices.



Qiang Yu obtained his Bachelor's degree in 2015 from the School of Materials Science and Engineering, Liaocheng University. He is now a Ph.D. candidate at Wuhan University of Technology with Prof. Liqiang Mai and Prof. Dongyuan Zhao. His research interests focus on the development of nanostructured carbon materials for application in supercapacitor and Lithium-ion battery.



Kaichun Yang received his Bachelor's degree in Department of Civil Engineering from Harbin Institute of Technology (HIT) in 2016. He is focusing on laser-induced graphene based nanocomposites and sensing devices for graduate study at Rice University.



Xufeng Hong received his Bachelor's degree in Department of Materials Science and Engineering from Wuhan University of Technology (WUT) in 2018. He is currently working toward the Master's degree. And his current focus is micro energy storage devices such as micro-supercapacitors and micro-batteries.



Liqiang Mai is Chair Professor of Materials Science and Engineering at Wuhan University of Technology (WUT). He is Changjiang Scholar Professor, Distinguished Young Scholar of the National Science Fund of China. He received his Ph.D. from WUT in 2004 and carried out his post-doctoral research in the laboratory of Prof. Zhonglin Wang at Georgia Institute of Technology in 2006–2007. He worked as advanced research scholar in the laboratory of Prof. Charles M. Lieber at Harvard University in 2008–2011 and Prof. Peidong Yang's group at University of California, Berkeley in 2017. His current research interests focus on nanomaterials and devices for energy storage.